ARTICLE

Open Access

Efficient photon-pair generation in layer-poled lithium niobate nanophotonic waveguides

Xiaodong Shi [1], Sakthi Sanjeev Mohanraj[1], Veerendra Dhyani[1], Angela Anna Baiju[1,2], Sihao Wang[1], Jiapeng Sun[3], Lin Zhou[4], Anna Paterova [1], Victor Leong [1] and Di Zhu [1,3,4 ✉]

Abstract

Integrated photon-pair sources are crucial for scalable photonic quantum systems. Thin-film lithium niobate is a promising platform for on-chip photon-pair generation through spontaneous parametric down-conversion (SPDC). However, the device implementation faces practical challenges. Periodically poled lithium niobate (PPLN), despite enabling flexible quasi-phase matching, suffers from poor fabrication reliability and device repeatability, while conventional modal phase matching (MPM) methods yield limited efficiencies due to inadequate mode overlaps. Here, we introduce a layer-poled lithium niobate (LPLN) nanophotonic waveguide for efficient photon-pair generation. It leverages layer-wise polarity inversion through electrical poling to break spatial symmetry and significantly enhance nonlinear interactions for MPM, achieving a notable normalized second-harmonic generation (SHG) conversion efficiency of 4615% $W^{-1}cm^{-2}$. Through a cascaded SHG and SPDC process, we demonstrate photon-pair generation with a normalized brightness of 3.1×10^6 Hz nm^{-1} mW^{-2} in a 3.3 mm long LPLN waveguide, surpassing existing on-chip sources under similar operating configurations. Crucially, our LPLN waveguides offer enhanced fabrication reliability and reduced sensitivity to geometric variations and temperature fluctuations compared to PPLN devices. We expect LPLN to become a promising solution for on-chip nonlinear wavelength conversion and non-classical light generation, with immediate applications in quantum communication, networking, and on-chip photonic quantum information processing.

Introduction

Correlated photon pairs are fundamental resources for photonic quantum technologies, from quantum communication and networking to sensing and computing[1–7]. They are usually generated through nonlinear optical processes such as spontaneous parametric down-conversion (SPDC) and spontaneous four-wave mixing (SpFWM). Integrated nanophotonic waveguides feature tight mode confinement and facilitate strong nonlinear interaction, making them well-suited for efficient photon-pair generations[8,9]. Moreover, their dense integration with various functional components in a compact chip is particularly promising for implementing scalable quantum information processors[10–12].

Common integrated photonic materials, such as silicon (Si) and silicon nitride (SiN$_x$), are centrosymmetric and lack intrinsic second-order ($\chi^{(2)}$) nonlinearity unless under special conditions like strain or strong DC field[13,14]. They typically rely on SpFWM for photon-pair generation. As a $\chi^{(3)}$ nonlinear process, SpFWM usually has limited nonlinear conversion efficiency and requires long waveguides, cavities, or pulsed pumps for practical applications[15–18]. In contrast, SPDC is a $\chi^{(2)}$ process and can achieve higher efficiency, but demands more stringent requirements. Specifically, SPDC involves photons at drastically different wavelengths (e.g., visible pump light is needed for telecom photon-pair generation), making phase matching challenging, especially in nanophotonic waveguides, where geometric dispersion is severe. Among various $\chi^{(2)}$ materials[19–23], thin-film lithium niobate (TFLN) stands out as an ideal platform. It has low loss, broad transparency

Correspondence: Di Zhu (dizhu@nus.edu.sg)
[1]A*STAR Quantum Innovation Centre (Q.InC), Institute of Materials Research and Engineering (IMRE), Agency for Science, Technology and Research (A*STAR), Singapore 138634, Singapore
[2]Department of Physics, National University of Singapore, Singapore 117542, Singapore
Full list of author information is available at the end of the article
These authors contributed equally: Xiaodong Shi, Sakthi Sanjeev Mohanraj.

window, large $\chi^{(2)}$ coefficient, and most crucially, ferroelectricity that enables electrical poling[24,25]. In TFLN, periodic poling is commonly adopted to achieve flexible quasi-phase matching (QPM) across different wavelengths. It has recently led to impressive results in efficient frequency conversion and non-classical light generation[19,26–28]. However, the fabrication reliability and device repeatability of periodically poled lithium niobate (PPLN) nanophotonic waveguides remain an outstanding challenge. The poling quality (poling depth and duty cycle) critically depends on the fabrication conditions (poling voltage, pulse duration, temperature, electrode geometry, etc.), and can affect the device performances (see Table S1 for a wide range of normalized nonlinear conversion efficiencies reported in the literature). In addition, PPLN waveguides' phase-matching functions are sensitive to structural inhomogeneities and temperatures[29–31]. Alternatively, modal phase matching (MPM) can achieve perfect phase matching by involving higher-order modes, where dispersions and matched wavelengths can be tailored by waveguide dimensions[32]. However, restricted by their symmetry properties, fundamental and higher-order modes have limited spatial overlap, resulting in relatively low nonlinear conversion efficiency.

This restriction can be resolved by breaking the spatial symmetry of the nonlinear media[33–36]. One implementation is to grow a layer of non-$\chi^{(2)}$ material (e.g., titanium oxide) on top of TFLN to form a "semi-nonlinear" waveguide[33]. However, in this case, only half of the guided mode contributes to $\chi^{(2)}$ interaction. To address this problem, double-layer TFLN waveguides have been proposed and demonstrated by direct bonding of two reversely oriented *x*-cut lithium niobate (LN) films[34,37–39]. This scheme has shown a measured second-harmonic generation (SHG) efficiency of up to 5540% $W^{-1}cm^{-2}$ and a higher theoretical SHG efficiency even exceeding that of QPM[37]. Despite its high efficiency, such directly bonded double-layer wafers face several practical issues. Firstly, it is incompatible with integrating other functional components on the same chip, such as electro-optic modulators. Secondly, it was observed that wet-chemical treatments in the fabrication could introduce discontinuities on the waveguide sidewalls due to the anisotropic etching of LN waveguides with opposite crystal orientations, resulting in a high scattering loss.

In this paper, we demonstrate efficient photon-pair generation in a modal-phase-matched TFLN nanophotonic waveguide with inversely polarized layers induced by electrical poling. The layer-wise poling process is robust and can be locally applied to individual devices on a chip. With the layer-poled lithium niobate (LPLN) waveguide, we measured a high normalized SHG efficiency of 4615 ± 82% $W^{-1}cm^{-2}$. Importantly, we
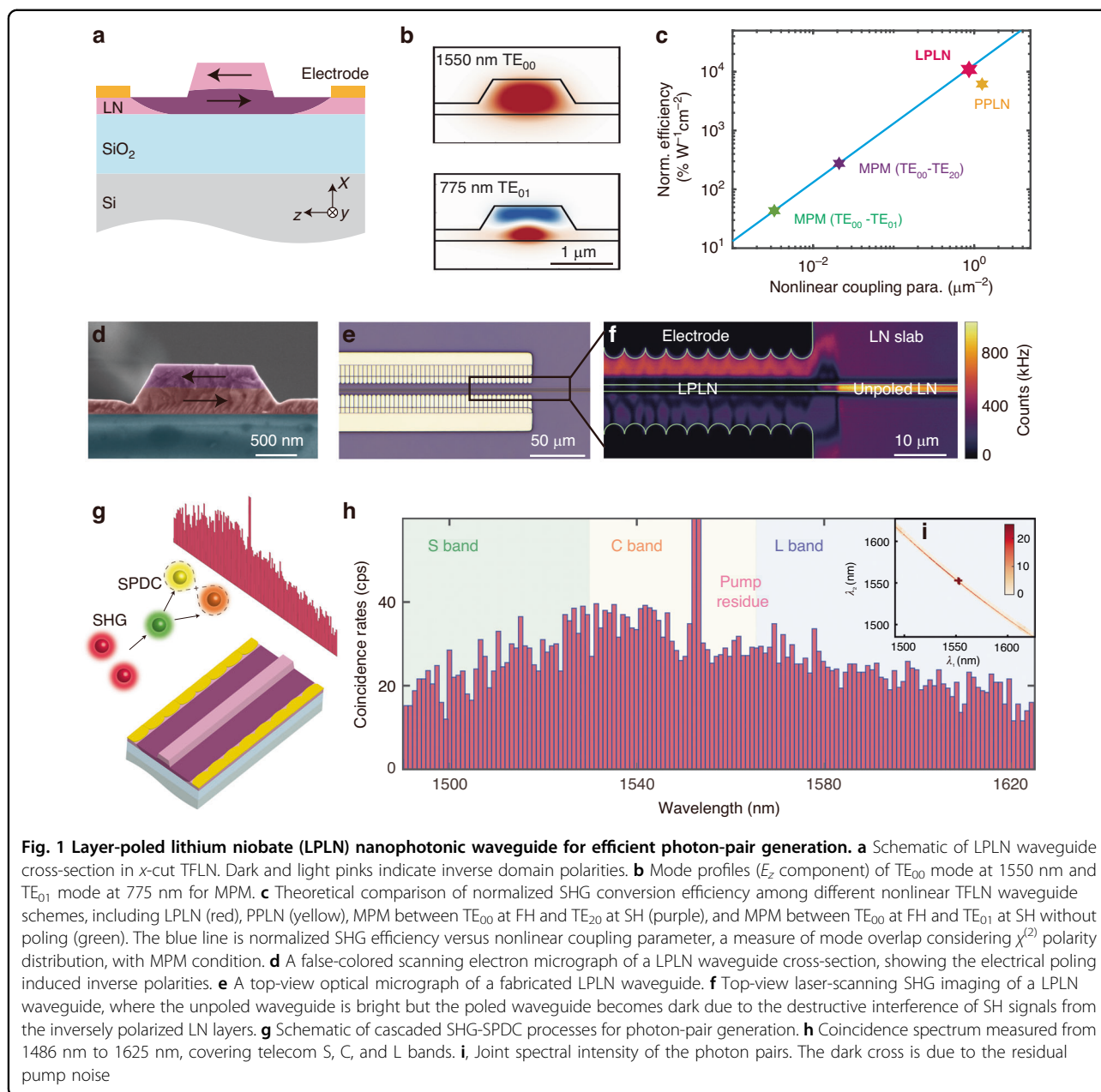
experimentally demonstrate efficient and broadband telecom photon-pair generation in a single LPLN waveguide through a cascaded SHG and SPDC scheme. This scheme only requires standard telecom components (such as telecom laser and dense wavelength division multiplexer) and eliminates the need for visible pump lasers or extra SHG modules[40–44]. In a 3.3 mm long LPLN waveguide, we observed broadband correlated photon pairs spanning the telecom S, C, and L bands, with a normalized brightness of 3.1 × 10⁶ Hz $nm^{-1}mW^{-2}$, which is among the highest achieved in nanophotonic waveguides with similar configurations. Our device is fabrication-friendly and comparatively more stable than PPLN against variations in waveguide geometry and temperature. The pair-generation scheme is simple and efficient, making our LPLN photon-pair source suitable for practical applications in quantum communication and networking, as well as integrated quantum photonic information processing.

Results
Device principle

Figure 1a shows the cross-section of the proposed LPLN waveguide, which is along the crystal y-axis in an x-cut LN. The LPLN waveguide is designed to have MPM between the 1550 nm fundamental transverse-electric mode (TE_{00}) and 775 nm first-order transverse-electric mode (TE_{01}), ultilizing the largest $\chi^{(2)}$ coefficient, d_{33}. Due to symmetry difference (Fig. 1b), in a homogeneous waveguide, these two modes should have near-zero overlap, resulting in negligible SHG conversion efficiency (see Fig. 1c, where we use simulated SHG efficiency as a measure to evaluate nonlinear efficiencies). To have non-zero overlap, one needs to use an even-order mode (e.g. TE_{20}) at 775 nm, but the mode overlap is non-optimal. Here, we break the spatial symmetry of the nonlinear material by creating layer-wise inverse polarities in x-cut TFLN rib waveguides through electrical poling. This is possible as the electric field from the surface poling electrode on the LN slab is more concentrated in the lower layer due to LN's high permittivity ($\epsilon_{r,z} = 28$). As a result, domain inversion initiates from the bottom part of the waveguides. Such layer-wise polarity inversion corrects for the symmetry mismatch between TE_{00} and TE_{01} modes, therefore enabling a large nonlinear mode overlap. Since MPM is perfect phase matching, the SHG efficiency can be higher than that of QPM, which has an intrinsic $(2/\pi)^2$ penalty in SHG efficiency despite near-optimal mode overlap[45].

Figure 1d shows a scanning electron micrograph of the cross-section of a fabricated LPLN waveguide. The false-color shading marks the layer-wise inverse polarities induced by electrical poling, extracted by intentionally immersing the waveguide in hydrofluoric acid and Standard

Fig. 1 Layer-poled lithium niobate (LPLN) nanophotonic waveguide for efficient photon-pair generation. a Schematic of LPLN waveguide cross-section in *x*-cut TFLN. Dark and light pinks indicate inverse domain polarities. **b** Mode profiles (E_z component) of TE_{00} mode at 1550 nm and TE_{01} mode at 775 nm for MPM. **c** Theoretical comparison of normalized SHG conversion efficiency among different nonlinear TFLN waveguide schemes, including LPLN (red), PPLN (yellow), MPM between TE_{00} at FH and TE_{20} at SH (purple), and MPM between TE_{00} at FH and TE_{01} at SH without poling (green). The blue line is normalized SHG efficiency versus nonlinear coupling parameter, a measure of mode overlap considering $\chi^{(2)}$ polarity distribution, with MPM condition. **d** A false-colored scanning electron micrograph of a LPLN waveguide cross-section, showing the electrical poling induced inverse polarities. **e** A top-view optical micrograph of a fabricated LPLN waveguide. **f** Top-view laser-scanning SHG imaging of a LPLN waveguide, where the unpoled waveguide is bright but the poled waveguide becomes dark due to the destructive interference of SH signals from the inversely polarized LN layers. **g** Schematic of cascaded SHG-SPDC processes for photon-pair generation. **h** Coincidence spectrum measured from 1486 nm to 1625 nm, covering telecom S, C, and L bands. **i**, Joint spectral intensity of the photon pairs. The dark cross is due to the residual pump noise

Clean 1 (SC-1) solution (a mixture of ammonium hydroxide and hydrogen peroxide) to induce polarity-dependent etching and reveal the poled layers (see Supplementary Fig. S1). Figure 1e shows an optical micrograph of the device, where we place electrodes with dense fingers for inducing a uniform electric field across the waveguide. With laser-scanning SHG microscopy, we observe that the poled section of the waveguide becomes dark (Fig. 1f). This is because the second-harmonic photons generated in the top and bottom layers of the LPLN waveguide are out of phase due to the reversed material polarity. These photons destructively interfere and cancel out in far-field imaging.

Laser-scanning SHG images for the LPLN waveguide before and after poling are shown in Supplementary Fig. S2, as well as one for a PPLN waveguide for comparison. We also observe that the LPLN poling is relatively insensitive to poling pulse settings (voltage and number of pulses; see Supplementary Fig. S3) and does not require elevated temperature or sharp electrodes (see Materials and methods), as compared to PPLN.

To create photon pairs, we directly pump a telecom continuous-wave (cw) laser through the LPLN waveguide at its phase-matching wavelength. As the telecom pump traverses the waveguide, it produces SHG light, which

generates SPDC simultaneously (Fig. 1g). Since the two processes happen in the same waveguide, the phase-matching wavelength for SHG and SPDC are automatically aligned. After filtering out the pump, we perform spectrally resolved coincidence counting using a pair of tunable filters and single-photon detectors. The photon pairs show strong frequency correlation and broad bandwidth extending the entire telecom S, C, and L bands, which is only limited by the tunable filter wavelength range (Fig. 1h, i).

Classical analysis of the nonlinear response of LPLN waveguides

Next, we quantitatively analyze the performances of the LPLN waveguide based on its SHG response. The phase-matching wavelength is controlled by tailoring the waveguide dimensions. Here, in a 600 nm thick TFLN waveguide with 400 nm etch depth, we find that a width of 1100 nm allows the 1550 nm TE_{00} mode to match 775 nm TE_{01} mode (see Supplementary Fig. S4).

When the phase-matching condition is fulfilled, the normalized SHG conversion efficiency in a lossless waveguide without pump depletion can be expressed as[46,47]

$$\eta = \frac{P_{SH}}{P_{FH}^2 L^2} = \frac{8\pi^2}{\epsilon_0 c n_{FH}^2 n_{SH} \lambda^2} d_{eff}^2 \Gamma \tag{1}$$

where P_{SH} is the generated second-harmonic (SH) power, P_{FH} is the pump power of the fundamental-harmonic (FH) wave, L is the length of the phase-matched waveguide, ϵ_0 is the free-space permittivity, c is the speed of light, λ is the FH wavelength, n is the effective index, and d_{eff} is the effective second-order nonlinear susceptibility ($d_{eff} = d_{33} = 27$ pm/V in this work). Γ is the nonlinear coupling parameter between the FH and SH modes taking into account the non-uniform $\chi^{(2)}$ distribution, given by

$$\Gamma = \frac{|\int_{LN} p(x,z) \cdot (E_{z,FH}^*)^2 E_{z,SH} dxdz|^2}{|\int_{all} |E_{FH}|^2 dxdz|^2 \int_{all} |E_{SH}|^2 dxdz} \tag{2}$$

where $p(x, z)$ denotes the $\chi^{(2)}$ polarity distribution, with $p = -1$ or 1 corresponding to polarity along $-z$ or $+z$ axis, respectively. Here, we only consider the overlap of the z-component of the electric fields (E_z) for the TE modes.

Based on numerical simulations, the nonlinear coupling parameter Γ between the 1550 nm TE_{00} mode and the 775 nm TE_{01} mode is improved by two orders of magnitude in a LPLN waveguide ($7.65 \times 10^{-1} \mu m^{-2}$ at an optimal poling depth of 290 nm, see Fig. 2a red dot) as compared to an unpoled one ($3.57 \times 10^{-3} \mu m^{-2}$, see Fig. 2a green dot). We also vary the poling depth and find a 3
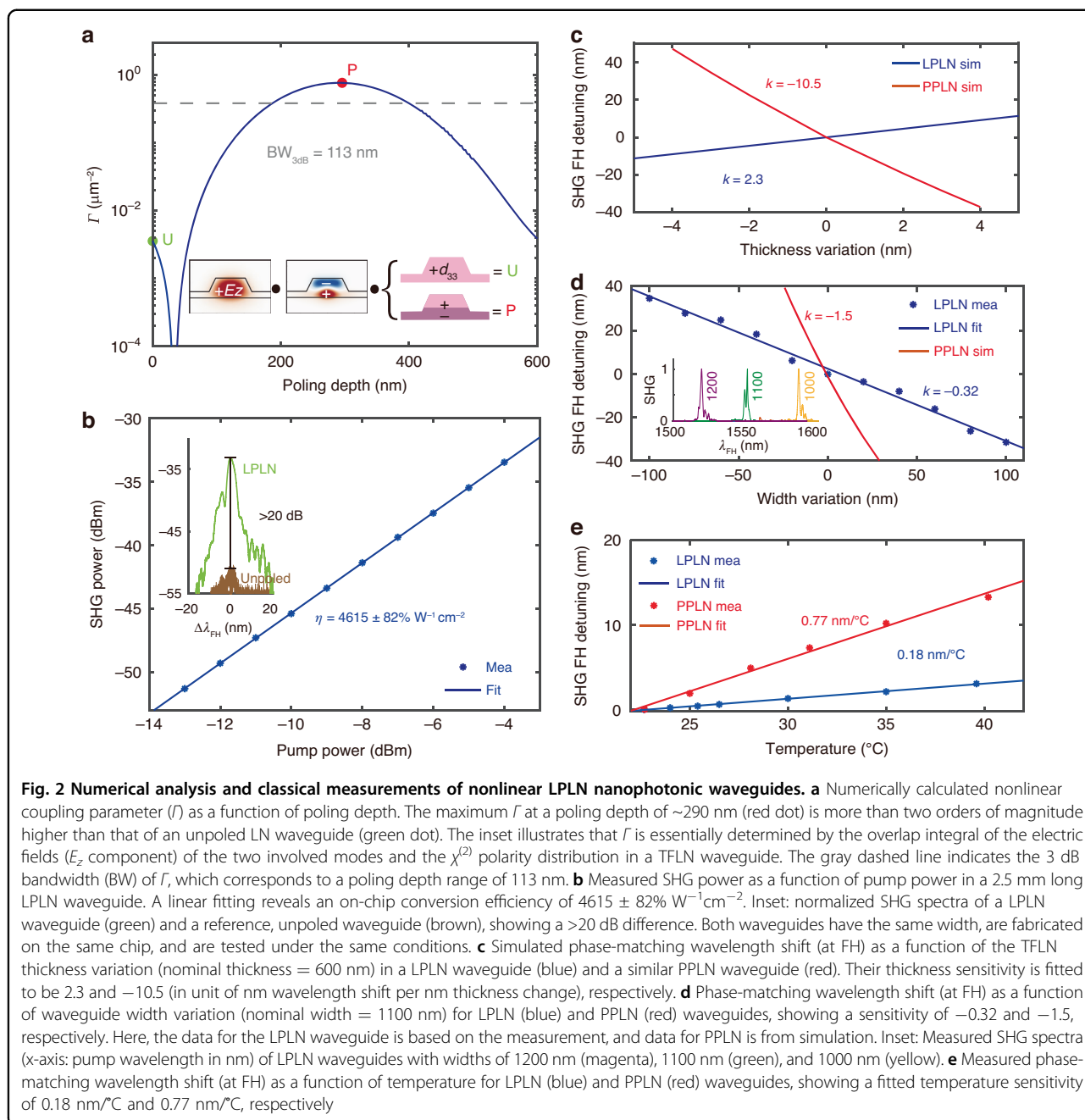
dB bandwidth of 113 nm, which is 39% of the optimal poling depth, suggesting that the nonlinear efficiency is reasonably tolerant against fabrication variations (Fig. 2a).

We further calculate the normalized SHG conversion efficiency in the LPLN waveguide (at the optimal poling depth) to be $\eta_{sim} = 1.01 \times 10^4\%$ $W^{-1}cm^{-2}$, which is about twice that in a QPM-based PPLN waveguide due to $(2/\pi)^2$ penalty, and two orders of magnitude higher than other MPM-based schemes (Fig. 1c). Thus, LPLN holds the promise of delivering the highest $\chi^{(2)}$ conversion efficiency among other types of TFLN waveguides.

We fabricate the LPLN nanophotonic waveguides using electron-beam lithography and dry etching, followed by electrical poling to obtain the layer-wise polarity inversion in the waveguides (see Materials and methods for fabrication details, and Fig. 1d, e for micrographs). Figure 2b shows the measured SHG power as a function of on-chip pump power in a 2.5 mm long LPLN nanophotonic waveguide. A linear fitting slope of 1.97 in the log-log plot confirms the quadratic relation between on-chip SH and FH powers in the undepleted-pump regime. We extract a normalized on-chip SHG conversion efficiency of $\eta_{exp} = 4615 \pm 82\%$ $W^{-1}cm^{-2}$. The measured conversion efficiency is lower than the theoretical prediction, likely due to variations in waveguide dimensions and the poling depth along the waveguide, which causes fluctuations in the optimal phase-matching wavelength and the nonlinear overlap parameter, respectively. Compared with other nonlinear LN nanophotonic waveguides, the LPLN waveguide generally performs high normalized SHG conversion efficiency (see Supplementary Table S1). The inset of Fig. 2b shows the measured SHG spectra of a LPLN waveguide and an unpoled reference waveguide fabricated on the same chip with the same waveguide dimensions. The LPLN waveguide shows over 20 dB higher SHG efficiency than the unpoled one, agreeing well with the theoretical predictions in Fig. 2a and Fig. 1c. One drawback of this scheme is that high-order modes are usually difficult to manipulate on chip or interface with single-mode fibers. If one wants to directly use SH light generated from the LPLN waveguides, microring/racetrack resonators can be used for mode conversion[48,49]. The modal-phase-matched second-order nonlinear interaction takes place in the resonator, and the high-order SH light can be coupled out from a single-mode add-drop waveguide at the fundamental mode.
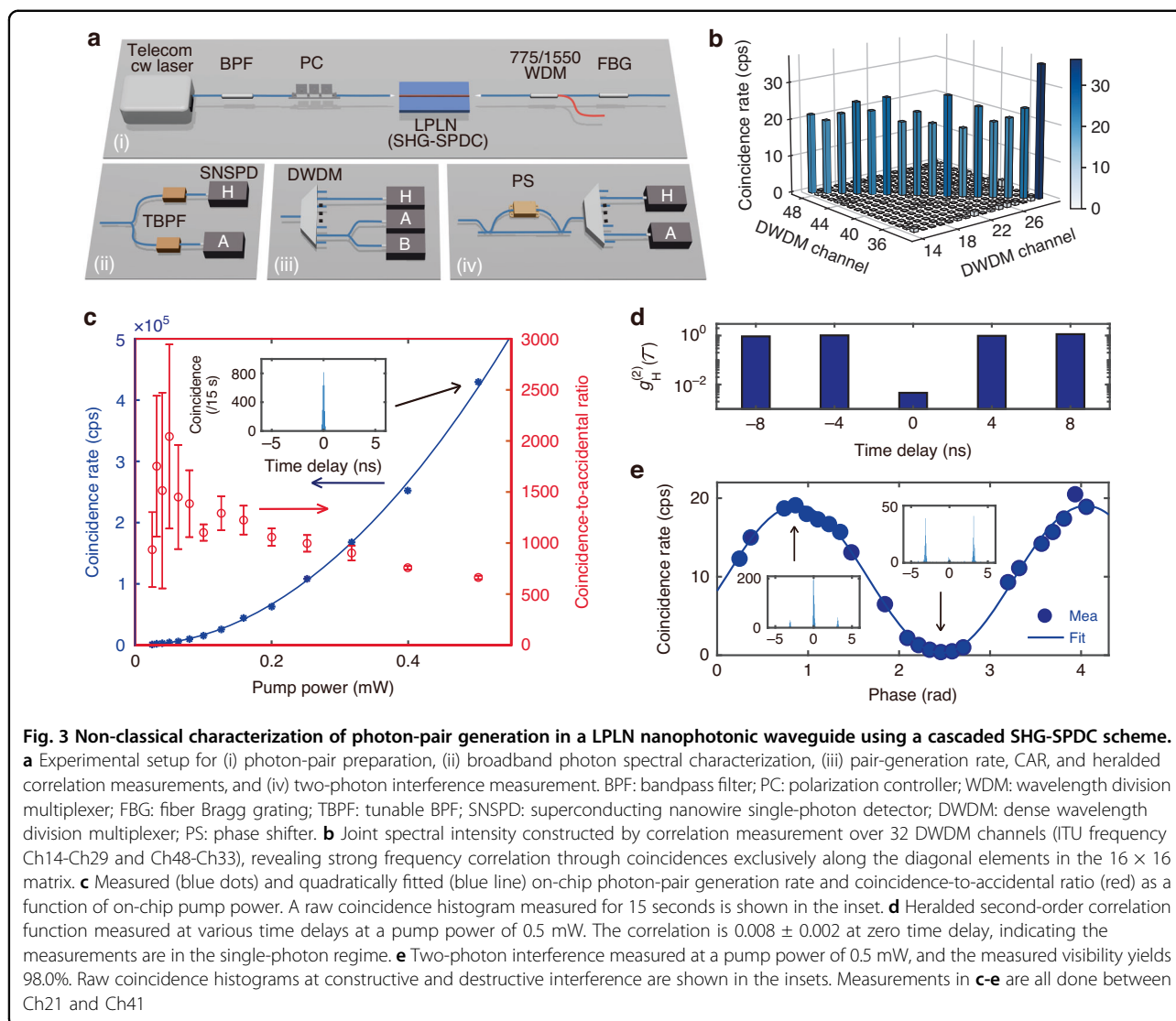
Comparative analysis of geometry and temperature sensitivity in LPLN and PPLN waveguides

A significant challenge in scaling up nanophotonic frequency converters or SPDC sources stems from the strong geometric dependence of phase-matching

Fig. 2 Numerical analysis and classical measurements of nonlinear LPLN nanophotonic waveguides. a Numerically calculated nonlinear coupling parameter (Γ) as a function of poling depth. The maximum Γ at a poling depth of ~290 nm (red dot) is more than two orders of magnitude higher than that of an unpoled LN waveguide (green dot). The inset illustrates that Γ is essentially determined by the overlap integral of the electric fields (E_z component) of the two involved modes and the $\chi^{(2)}$ polarity distribution in a TFLN waveguide. The gray dashed line indicates the 3 dB bandwidth (BW) of Γ, which corresponds to a poling depth range of 113 nm. **b** Measured SHG power as a function of pump power in a 2.5 mm long LPLN waveguide. A linear fitting reveals an on-chip conversion efficiency of 4615 ± 82% W^{-1}cm^{-2}. Inset: normalized SHG spectra of a LPLN waveguide (green) and a reference, unpoled waveguide (brown), showing a >20 dB difference. Both waveguides have the same width, are fabricated on the same chip, and are tested under the same conditions. **c** Simulated phase-matching wavelength shift (at FH) as a function of the TFLN thickness variation (nominal thickness = 600 nm) in a LPLN waveguide (blue) and a similar PPLN waveguide (red). Their thickness sensitivity is fitted to be 2.3 and −10.5 (in unit of nm wavelength shift per nm thickness change), respectively. **d** Phase-matching wavelength shift (at FH) as a function of waveguide width variation (nominal width = 1100 nm) for LPLN (blue) and PPLN (red) waveguides, showing a sensitivity of −0.32 and −1.5, respectively. Here, the data for the LPLN waveguide is based on the measurement, and data for PPLN is from simulation. Inset: Measured SHG spectra (x-axis: pump wavelength in nm) of LPLN waveguides with widths of 1200 nm (magenta), 1100 nm (green), and 1000 nm (yellow). **e** Measured phase-matching wavelength shift (at FH) as a function of temperature for LPLN (blue) and PPLN (red) waveguides, showing a fitted temperature sensitivity of 0.18 nm/°C and 0.77 nm/°C, respectively

wavelengths[31]. This dependency makes the fabrication of devices with identical phase-matching wavelengths difficult. In this section, we compare the SHG phase-matching sensitivity of LPLN and PPLN waveguides. We first evaluate how the phase-matching wavelength changes as a function of TFLN thickness in a LPLN waveguide, and find that thicker films result in longer phase-matching wavelengths, with a simulated rate of 2.3 nm redshift per nm of thickness increase (Fig. 2c). This rate is approximately 5 times lower than that of PPLN waveguides, which has a simulated rate of 10.5 nm blueshift per nm of

thickness increment. We then measure the SHG spectra of a series of LPLN waveguides with the same length but different widths (from 1000 nm to 1200 nm in 20 nm increments) and extract their phase-matching wavelengths. We observe that narrower waveguides have longer phase-matching wavelengths, with a measured rate of 0.32 nm redshift per nm of width reduction (Fig. 2d). The inset of Fig. 2d shows the exemplary SHG spectra with waveguide widths of 1200 nm, 1100 nm, and 1000 nm. The asymmetry and broadening in the measured SHG spectra are likely due to the non-uniformity in the

Fig. 3 Non-classical characterization of photon-pair generation in a LPLN nanophotonic waveguide using a cascaded SHG-SPDC scheme.
a Experimental setup for (i) photon-pair preparation, (ii) broadband photon spectral characterization, (iii) pair-generation rate, CAR, and heralded correlation measurements, and (iv) two-photon interference measurement. BPF: bandpass filter; PC: polarization controller; WDM: wavelength division multiplexer; FBG: fiber Bragg grating; TBPF: tunable BPF; SNSPD: superconducting nanowire single-photon detector; DWDM: dense wavelength division multiplexer; PS: phase shifter. **b** Joint spectral intensity constructed by correlation measurement over 32 DWDM channels (ITU frequency Ch14-Ch29 and Ch48-Ch33), revealing strong frequency correlation through coincidences exclusively along the diagonal elements in the 16×16 matrix. **c** Measured (blue dots) and quadratically fitted (blue line) on-chip photon-pair generation rate and coincidence-to-accidental ratio (red) as a function of on-chip pump power. A raw coincidence histogram measured for 15 seconds is shown in the inset. **d** Heralded second-order correlation function measured at various time delays at a pump power of 0.5 mW. The correlation is 0.008 ± 0.002 at zero time delay, indicating the measurements are in the single-photon regime. **e** Two-photon interference measured at a pump power of 0.5 mW, and the measured visibility yields 98.0%. Raw coincidence histograms at constructive and destructive interference are shown in the insets. Measurements in **c-e** are all done between Ch21 and Ch41

width and height of the LPLN waveguides. The phase-matching sensitivity against waveguide width measured here (-0.32) is about 5 times smaller than that in the PPLN waveguide (simulated to be -1.5). These results suggest that, compared to PPLN waveguides, LPLN waveguides exhibit reduced sensitivity to geometric variations.

We further characterize the thermal stability of LPLN waveguides and compare it with PPLN waveguides (also fabricated on a 600 nm thick x-cut TFLN). We tune the temperature from 23 °C to 40 °C and measure the corresponding SHG phase-matching wavelengths in both LPLN and PPLN waveguides (Fig. 2e). Both waveguides show redshifts with increasing temperature. The measured thermal shifting slope of the LPLN waveguide is 0.18 nm/°C, about four times smaller than that of the PPLN waveguide (0.77 nm/°C), suggesting better thermal stability.

Photon-pair generation *via* cascaded SHG and SPDC

Finally, we use a 3.3 mm long LPLN nanophotonic waveguide for photon-pair generation through a cascaded SHG-SPDC process. Here, we couple a cw laser at 1552.52 nm to the chip using a lensed fiber. This wavelength matches the waveguide's phase-matching point and also corresponds to the International Telecommunication Union (ITU) channel, Ch31. The output is coupled back into a fiber and passed through a 775 nm/1550 nm wavelength division multiplexer (WDM) to filter out the SHG light and a fiber Bragg grating (FBG) for telecom pump filtering (Fig. 3a(i)).

We characterize the photon-pair bandwidth by splitting the output into a pair of tunable band-pass filters ($\Delta\lambda_{\text{FWHM}} = 0.6$ nm) and measuring the coincidence counts as a function of wavelengths using super-conducting nanowire single-photon detectors (SNSPDs,

see Fig. 3a(ii)). Figure 1i shows the measured joint spectrum intensity, and Fig. 1h shows the measured spectrum of the photon pairs from 1486 nm to 1625 nm, covering the telecom S, C, and L bands. Such broad bandwidth benefits from the low group velocity dispersion in the LPLN waveguide, resulting in a diagonally oriented phase-matching function[19], which is confirmed through the sum-frequency generation (SFG) measurement (see Supplementary Fig. S5).

The broadband telecom photon-pair source is well suited for wavelength-multiplexed quantum networks. Here, we connect the device output to a commercial dense wavelength division multiplexer (DWDM) that matches the standard ITU frequency grid, dividing the broadband source into 32 wavelength channels. Figure 3b shows the measured 16×16 matrix that describes the correlations among different wavelength channels. The correlation appears only along the diagonal elements of the matrix, demonstrating a characteristic feature of a high-dimensional quantum state and strong frequency correlation.

We pick Ch21 and Ch41, which are spectrally symmetric to the pump wavelength (Ch31), and perform detailed characterizations of the on-chip pair generation rate (PGR) and coincidence-to-accidental ratio (CAR) as a function of the pump power (Fig. 3c). Here, the on-chip PGR is extracted by factoring out the losses from fiber-chip coupling, filters, DWDM, and detector inefficiencies. It scales quadratically to pump power and reaches 0.43 Mcps at an on-chip pump power of 0.5 mW. Based on the measured channel bandwidth of $\Delta\lambda_{\mathrm{FWHM}} = 0.56$ nm (see Supplementary Fig. S6), we estimate the normalized brightness of the photon-pair source to be $B = \frac{\mathrm{PGR}}{\Delta\lambda_{\mathrm{FWHM}} P_{\mathrm{pump}}^2} = 3.1 \times 10^6$ Hz nm^{-1} mW^{-2}, where P_{pump} is the pump power and $\Delta\lambda_{\mathrm{FWHM}}$ is the full-width at half-maximum (FWHM) of the signal and idler channels. The highest CAR reaches 2043 ± 902 at 0.05 mW pump power (PGR = 4.4 kcps). At low pump power, the CAR is limited by dark counts; and at high pump power, it is limited by multi-photon events, Raman scattering, and residual pump photons.

SPDC sources can be used to generate heralded single photons. We test the photon-number purity of the source by performing heralded second-order correlation measurement, using the detection setup in Fig. 3a(iii). We send the signal photons (Ch21) into a heralding detector (H) and split the idler photons (Ch41) using a 50/50 beamsplitter and measure the coincidence as a function of time delay (τ) between the two detectors (A and B). The heralded second-order correlation is given by $g_{\mathrm{H}}^{(2)}(\tau) = \frac{N_{\mathrm{H}} N_{\mathrm{HAB}}(\tau)}{N_{\mathrm{HA}}(\tau) N_{\mathrm{HB}}(\tau)}$, where N_{H} is the photon counts on detector H, $N_{\mathrm{HA/HB}}$ is the coincidence counts between detector H and A/B, and N_{HAB} is the triple coincidence events among three detectors (H, A, and B)[50]. Figure 3d shows the

measured $g_{\mathrm{H}}^{(2)}(\tau)$ at a pump power of 0.5 mW, where a clear anti-bunching dip with $g_{\mathrm{H}}^{(2)}(0) = 0.008 \pm 0.002$ is observed, corresponding to a photon-number purity of $P = 1 - g_{\mathrm{H}}^{(2)}(0) = 99.2\%$[51]. A lower $g_{\mathrm{H}}^{(2)}(0)$ is expected at lower pump power due to reduced noise photons and lower multi-photon probability. Note that the strong spectral correlation of the type-0 SPDC source results in low spectral purity of the heralded single photons[52]. This will limit their indistinguishability for applications that require high Hong-Ou-Mandel interference visibility. To achieve high spectral purity, narrow spectral filtering or type-II, pulsed-pumped schemes are needed[53,54].

The cw-pumped SPDC photon pairs are naturally energy-time entangled and can be a useful resource for quantum communications. We perform Franson-like two-photon interference using an unbalanced Mach-Zehnder interferometer (MZI) to coherently manipulate the two-photon quantum states by applying a phase shift using a fiber stretcher (Fig. 3a(iv))[40]. The zero-delay coincidence shows a sinusoidal relation to the phase shift, exhibiting a periodic transition between bunched and anti-bunched states (Fig. 3e). The high visibility of 98.0% indicates high-quality energy-time entanglement of the photon pairs generated from the LPLN waveguide.

Discussion

We benchmark our results against other reported on-chip telecom photon-pair sources produced in nanophotonic waveguides using telecom cw pump, which so far are all based on SpFWM. The comparison in terms of brightness, CAR, and $g_{\mathrm{H}}^{(2)}(0)$ is shown in Table 1. We also compare the normalized brightness that accounts for the quadratic dependence of the PGR on the pump power,

Table 1 Comparison of photon-pair sources produced in a single waveguide with a telecom cw pump

Platform	L	P	Brightness	Normalized brightness	CAR	$g_{\mathrm{H}}^{(2)}(0)$
	(mm)	(mW)	(Hz nm^{-1})	(Hz nm^{-1} mW^{-2})		
Si[55]	11.3	5	2.0×10^6	7.8×10^4	4	-
Si[56]	8	11.2	7.1×10^6	5.7×10^4	251	0.014
Si[57]	10	1	1.9×10^5	1.9×10^5	~400	<0.12
SiN[58]	10	5.0	4.8×10^5	1.9×10^4	3	-
As$_2$S$_3$[18]	71	57	2.5×10^6	7.5×10^2	< 2	-
AlGaAs[59]	3	0.354	1.1×10^3	8.8×10^3	21	-
This work	3.3	0.5	7.7×10^5	3.1×10^6	663	0.008

Main factors include device length (*L*), pump power (*P*), brightness, normalized brightness, as well as coincidence-to-accidental ratio (CAR) and heralded second-order correlation ($g_{\mathrm{H}}^{(2)}(0)$) at the corresponding brightness

which is valid for both SpFWM and cascaded SHG-SPDC. Despite its short length of 3.3 mm, our LPLN waveguide shows the highest normalized brightness while simultaneously achieving high CAR and low $g_{\rm H}^{(2)}(0)$. Considering that the PGR of the cascaded SHG-SPDC scheme is quartic to the waveguide length (see derivation in Supplementary S3) while that in SpFWM scales quadratically, we can expect drastically improved pair generation efficiency in future longer LPLN devices.

Besides $\chi^{(2)}$, LN also possesses $\chi^{(3)}$ nonlinearity, which could contribute to photon-pair generation through SpFWM. To isolate this contribution, we shift the pump wavelength by ~6 nm away from the SHG phase-matching wavelength, ensuring that the SHG-induced SPDC becomes negligible and all measured photon pairs are from SpFWM. We observe that the PGR from SpFWM is about two orders of magnitude lower than that from the cascaded SHG-SPDC (see Supplementary Fig. S7). Therefore, the measured photon pairs in Fig. 3 are predominantly from the cascaded SHG-SPDC process (~99%).

We also experimentally compare the cascaded SHG-SPDC scheme with photon-pair generation using two separate LNPN chips, one for SHG and the other for SPDC (see Supplementary Fig. S8). The two-chip scheme allows more complete pump filtering, which results in a higher measured CAR approaching 4000. However, the SPDC generation efficiency is very sensitive to the optical coupling between the two chips, which is especially difficult since the SH light is in a high-order mode. Overall, the cascaded SHG-SPDC in a single waveguide requires a simpler setup and avoids inter-chip coupling losses and mismatched phase-matching conditions.

In summary, we have developed a LPLN nanophotonic waveguide for efficient $\chi^{(2)}$ nonlinear wavelength conversion and photon-pair generation. The LPLN photon-pair source, which operates under a cascaded SHG-SPDC scheme, is broadband and features high normalized brightness, high CAR, and low heralded $g_{\rm H}^{(2)}(0)$, outperforming other photon-pair sources in nanophotonic waveguides using telecom cw pumps. Compared with traditional PPLN, the LPLN waveguide requires a simpler poling process with larger error tolerance, and its phase-matching wavelength is less sensitive to waveguide geometry and temperature variations. We anticipate that LPLN will be a suitable method for the future scalable production of integrated nonlinear and quantum light sources, with immediate applications in quantum communications and on-chip photonic quantum information processing.

Materials and methods
Numerical simulation
The waveguide effective indices and mode distributions are simulated numerically using a finite difference mode solver (Ansys Lumerical MODE). For the MPM design, we target phase matching between 1550 nm TE_{00} and 775 nm TE_{01} modes. We design the waveguides based on a 600 nm thick x-cut TFLN with an etching depth of 400 nm and an etching angle of 60°. By tailoring the waveguide width, the two modes can have matched effective index (see Supplementary Fig. S4). For PPLN waveguide simulation shown in Fig. 2c, d, we adopt the same waveguide dimension as the LPLN waveguide and keep the poling period fixed for quasi-phase matching at the corresponding zero parameter variation with phase-matching wavelength at 1550 nm, to have fair comparison with the LPLN waveguide.

Device fabrication
We fabricate the LPLN waveguides in a 600 nm thick MgO-doped x-cut TFLN chip. The waveguides are patterned using electron-beam (e-beam) lithography and Ar^{+} etching by inductively coupled plasma reactive ion etching (ICP-RIE), with hydrogen silsesquioxane (HSQ) e-beam resist as the etching mask. An 80 nm thick SiO_2 layer is deposited using ICP chemical vapor deposition (ICP-CVD) as a buffer layer for poling. Round-tip comb-like electrodes with a pitch of 4 μm and duty cycle of 90% are patterned using a combination of e-beam and photon lithography, followed by e-beam metal evaporation (60 nm Ni/60 nm Cr) and lift-off. We apply a series of six 600 V, 4 ms-long electrical pulses to reverse the layer-wise polarity for LPLN waveguides, and the poling is performed at room temperature. After poling, the SiO_2 buffer layer is removed using hydrofluoric acid. A cross-section scanning electron micrograph and a top-view optical micrograph of a fabricated LPLN nanophotonic waveguide are shown in Fig. 1d and e, respectively.

Experimental details for classical characterizations
To extract the SHG conversion efficiency, we calibrate the fiber-to-chip coupling loss at 1550 nm using a pair of lensed fibers, and estimated the coupling loss to be 4.9 dB/facet. To measure the SHG power at 775 nm, we directly place a free-space-coupled visible-wavelength power meter (Si photodetector) at the chip output facet, and we assume negligible coupling loss here. We confirm that the Si photodetector is insensitive to the IR pump, and there is negligible third-harmonic or higher-harmonic generation during the SHG measurement. Figure 2b is measured by fixing the wavelength of the cw pump laser at the phase-matching point of the LPLN (i.e., the peak wavelength of the SHG spectrum in the inset), sweeping the laser power, and measuring the SHG power using the Si photodetector. Both the pump power and the SHG power are on-chip power. The average normalized conversion efficiency is calculated based on all the measured points shown in Fig. 2b, and the uncertainty is the

corresponding standard deviation. The SHG spectra shown in the insets of Fig. 2b, d are measured by synchronized sweeping of the tunable telecom pump laser while reading the Si photodetector using a data acquisition board.

Experimental setup for quantum characterizations

We use the experimental setups shown in Fig. 3a to characterize the cascaded SHG-SPDC photon-pair source. Figure 3a(i) shows the setup for photon-pair generation. A tunable telecom cw laser (Santec TLS-570) is used as the pump to stimulate the cascaded SHG-SPDC process, and its wavelength is set to 1552.52 nm, matching the SHG phase-matching wavelength and ITU Ch31. The side-band noise from the laser is suppressed through a bandpass filter. The pump is adjusted to be TE polarized using a polarization controller (PC) before launching into the waveguide. After the cascaded SHG-SPDC process in the LPLN waveguide, the pump, SHG light, and the generated photon pairs are coupled out of the chip together using a lensed fiber. No temperature control is used during the measurements. The SHG and pump light are filtered out through 1550 nm/ 775 nm WDM and FBG, respectively. For broadband photon-pair characterization in Fig. 1h, i, we use the detection setup shown in Fig. 3a(ii). The photon pairs are separated into two paths using a 50/50 beamsplitter, selected by two tunable BPFs (TBPF), and launched into two SNSPDs (ID Quantique ID281) for coincidence counting. During the measurement, the TBPF bandwidth is set to be 0.6 nm, and their center wavelengths sweep symmetrically to the pump wavelength. For the narrow-band photon-pair characterization in Fig. 3b–d, we use the detection setup shown in Fig. 3a(iii). Signal and idler photons are separated by DWDM with Ch21 and Ch41. For coincidence counting, signal and idler photons are measured by two SNSPDs, H and A. Cascaded BPFs are used to filter the signal and idler photons to further suppress the residual pump photons. Polarization controllers are used to optimize the photon polarization before launching into the SNSPDs in every path. The total loss for signal and idler photons is calibrated to be 18.2 dB and 16.8 dB, respectively, by measuring fiber-chip coupling loss, optical component insertion losses, and SNSPD detection inefficiencies, in order to predict the on-chip PGR in Fig. 3c. For the heralded second-order correlation measurement, the idler photons are separated into two paths (A and B) through a 50/50 beamsplitter. Both paths are launched into SNSPDs for photon detection, together with the signal photons (H). A virtual electrical time delay is added to path B in the time tagger (Swabian Time Tagger Ultra). For the two-photon interference characterization in Fig. 3e, we use the detection setup shown

in Fig. 3a(iv). Before separating the signal and idler photons for coincidence counting, the photon pairs go through an unbalanced Mach-Zehnder interferometer (MZI) with a fiber-stretcher-based phase shifter (PS) in one arm.

Author details
[1]A*STAR Quantum Innovation Centre (Q.InC), Institute of Materials Research and Engineering (IMRE), Agency for Science, Technology and Research (A*STAR), Singapore 138634, Singapore. [2]Department of Physics, National University of Singapore, Singapore 117542, Singapore. [3]Department of Materials Science and Engineering, National University of Singapore, Singapore 117575, Singapore. [4]Centre for Quantum Technologies, National University of Singapore, Singapore 117543, Singapore

Author contributions
D.Z., X.S. and S.S.M conceived the idea. X.S. and J.S. designed the devices. S.S.M. and V.D. fabricated the devices. X.S., A.A.B. and S.W. performed the measurements with the help of D.Z., V.L. and A.P. L.Z. and D.Z. did theoretical analysis. D.Z., V.L. and A.P. supervised the project. All the authors discussed the results and wrote the manuscript.

Conflict of interest
The authors declare no competing interests.

References
1. Wengerowsky, S., Joshi, S. K, Steinlechner, F., Hübel, H. & Ursin, R. An entanglement-based wavelength-multiplexed quantum communication network. *Nature* **564**, 225–228 (2018).
2. Zheng, Y. et al. Multichip multidimensional quantum networks with entanglement retrievability. *Science* **381**, 221–226 (2023).
3. Xiang, G.-Y., Higgins, B. L., Berry, D., Wiseman, H. M. & Pryde, G. Entanglement-enhanced measurement of a completely unknown optical phase. *Nat. Photonics* **5**, 43–47 (2011).
4. Kok, P. et al. Linear optical quantum computing with photonic qubits. *Rev. Mod. Phys.* **79**, 135 (2007).
5. Kues, M. et al. On-chip generation of high-dimensional entangled quantum states and their coherent control. *Nature* **546**, 622–626 (2017).
6. Couteau, C. et al. Applications of single photons to quantum communication and computing. *Nat. Rev. Phys.* **5**, 326–338 (2023).
7. Flamini, F., Spagnolo, N. & Sciarrino, F. Photonic quantum information processing: a review. *Rep. Prog. Phys.* **82**, 016001 (2018).
8. Wang, Y., Jöns, K. D. & Sun, Z. Integrated photon-pair sources with nonlinear optics. *Appl. Phys. Rev.* **8**, 011314 (2021).
9. Moody, G., Chang, L., Steiner, T. J. & Bowers, J. E. Chip-scale nonlinear photonics for quantum light generation. *AVS Quant. Sci.* **2**, 041702 (2020).

10. Wang, J. et al. Multidimensional quantum entanglement with large-scale integrated optics. *Science* **360**, 285–291 (2018).

11. Wang, J., Sciarrino, F., Laing, A. & Thompson, M. G. Integrated photonic quantum technologies. *Nat. Photonics* **14**, 273–284 (2020).

12. Pelucchi, E. et al. The potential and global outlook of integrated photonics for quantum technologies. *Nat. Rev. Phys.* **4**, 194–208 (2022).

13. Jacobsen, R. S. et al. Strained silicon as a new electro-optic material. *Nature* **441**, 199–202 (2006).

14. Zabelich, B., Nitiss, E., Stroganov, A. & Bres, C.-S. Linear electro-optic effect in silicon nitride waveguides enabled by electric-field poling. *ACS Photonics* **9**, 3374–3383 (2022).

15. Shi, X. et al. Multichannel photon-pair generation with strong and uniform spectral correlation in a silicon microring resonator. *Phys. Rev. Appl.* **12**, 034053 (2019).

16. Spring, J. B. et al. On-chip low loss heralded source of pure single photons. *Opt. Express* **21**, 13522–13532 (2013).

17. Xiong, C. et al. Compact and reconfigurable silicon nitride time-bin entanglement circuit. *Optica* **2**, 724–727 (2015).

18. Xiong, C. et al. Generation of correlated photon pairs in a chalcogenide as2s3 waveguide. *Appl. Phys. Lett.* **98**, 051101 (2011).

19. Javid, U. A. et al. Ultrabroadband entangled photons on a nanophotonic chip. *Phys. Rev. Lett.* **127**, 183601 (2021).

20. Guo, X. et al. Parametric down-conversion photon-pair source on a nanophotonic chip. *Light Sci. Appl.* **6**, e16249–e16249 (2017).

21. Li, J., Zhang, Q., Wang, J. & Poon, A. W. An integrated 3c-silicon carbide-on-insulator photonic platform for nonlinear and quantum light sources. *Commun. Phys.* **7**, 125 (2024).

22. Horn, R. et al. Monolithic source of photon pairs. *Phys. Rev. Lett.* **108**, 153605 (2012).

23. Autebert, C. et al. Integrated algaas source of highly indistinguishable and energy-time entangled photons. *Optica* **3**, 143–146 (2016).

24. Zhu, D. et al. Integrated photonics on thin-film lithium niobate. *Adv. Opt. Photonics* **13**, 242–352 (2021).

25. Saravi, S., Pertsch, T. & Setzpfandt, F. Lithium niobate on insulator: An emerging platform for integrated quantum photonics. *Adv. Opt. Mater.* **9**, 2100789 (2021).

26. Lu, J. et al. Periodically poled thin-film lithium niobate microring resonators with a second-harmonic generation efficiency of 250,000%/w. *Optica* **6**, 1455–1460 (2019).

27. Hwang, A. Y. et al. Mid-infrared spectroscopy with a broadly tunable thin-film lithium niobate optical parametric oscillator. *Optica* **10**, 1535–1542 (2023).

28. Park, T. et al. Single-mode squeezed-light generation and tomography with an integrated optical parametric oscillator. *Sci. Adv.* **10**, eadl1814 (2024).

29. Zhao, J. et al. Unveiling the origins of quasi-phase matching spectral imperfections in thin-film lithium niobate frequency doublers. *APL Photon.* **8**, 126106 (2023).

30. Chen, P.-K. et al. Adapted poling to break the nonlinear efficiency limit in nanophotonic lithium niobate waveguides. *Nat. Nanotechnol.* **19**, 44–50 (2024).

31. Xin, C. et al. Wavelength-accurate and wafer-scale process for nonlinear frequency mixers in thin-film lithium niobate. arXiv preprint arXiv:2404.12381 (2024).

32. Wang, C. et al. Second harmonic generation in nano-structured thin-film lithium niobate waveguides. *Opt. Express* **25**, 6963–6973 (2017).

33. Luo, R., He, Y., Liang, H., Li, M. & Lin, Q. Semi-nonlinear nanophotonic waveguides for highly efficient second-harmonic generation. *Laser Photon. Rev.* **13**, 1800288 (2019).

34. Zhang, X. et al. Antisymmetric-nonlinear lnoi waveguide for highly efficient second-harmonic generation. In *Asia Communications and Photonics Conference*, M4A–29 (Optica Publishing Group, 2020).

35. Gromovyi, M. et al. Intrinsic polarity inversion in iii-nitride waveguides for efficient nonlinear interactions. *Opt. Express* **31**, 31397–31409 (2023).

36. Cai, L., Gorbach, A. V., Wang, Y., Hu, H. & Ding, W. Highly efficient broadband second harmonic generation mediated by mode hybridization and nonlinearity patterning in compact fiber-integrated lithium niobate nano-waveguides. *Sci. Rep.* **8**, 12478 (2018).

37. Wang, L., Zhang, X. & Chen, F. Efficient second harmonic generation in a reverse-polarization dual-layer crystalline thin film nanophotonic waveguide. *Laser Photonics Rev.* **15**, 2100409 (2021).

38. Du, H., Zhang, X., Wang, L. & Chen, F. Highly efficient, modal phase-matched second harmonic generation in a double-layered thin film lithium niobate waveguide. *Opt. Express* **31**, 9713–9726 (2023).

39. Du, H., Zhang, X., Wang, L., Jia, Y. & Chen, F. Tunable sum-frequency generation in modal phase-matched thin film lithium niobate rib waveguides. *Opt. Lett.* **48**, 3159–3162 (2023).

40. Zhang, Z. et al. High-performance quantum entanglement generation via cascaded second-order nonlinear processes. *npj Quantum Inf.* **7**, 123 (2021).

41. Arahira, S., Namekata, N., Kishimoto, T. & Inoue, S. Experimental studies in generation of high-purity photon-pairs using cascaded $\chi^{(2)}$ processes in a periodically poled linbo 3 ridge-waveguide device. *JOSA B* **29**, 434–442 (2012).

42. Arahira, S., Namekata, N., Kishimoto, T., Yaegashi, H. & Inoue, S. Generation of polarization entangled photon pairs at telecommunication wavelength using cascaded $\chi^{(2)}$ processes in a periodically poled linbo$_3$ ridge waveguide. *Opt. Express* **19**, 16032–16043 (2011).

43. Hunault, M., Takesue, H., Tadanaga, O., Nishida, Y. & Asobe, M. Generation of time-bin entangled photon pairs by cascaded second-order nonlinearity in a single periodically poled linbo 3 waveguide. *Opt. Lett.* **35**, 1239–1241 (2010).

44. Elkus, B. S., Abdelsalam, K., Fathpour, S., Kumar, P. & Kanter, G. S. Quantum-correlated photon-pair generation via cascaded nonlinearity in an ultra-compact lithium-niobate nano-waveguide. *Opt. Express* **28**, 39963–39975 (2020).

45. Wang, C. et al. Ultrahigh-efficiency wavelength conversion in nanophotonic periodically poled lithium niobate waveguides. *Optica* **5**, 1438–1441 (2018).

46. Pliska, T., Fluck, D., Günter, P., Beckers, L. & Buchal, C. Linear and nonlinear optical properties of knbo 3 ridge waveguides. *J. Appl. Phys.* **84**, 1186–1195 (1998).

47. Stanton, E. J. et al. Efficient second harmonic generation in nanophotonic gaas-on-insulator waveguides. *Opt. Express* **28**, 9521–9532 (2020).

48. Guo, X., Zou, C.-L. & Tang, H. X. Second-harmonic generation in aluminum nitride microrings with 2500%/w conversion efficiency. *Optica* **3**, 1126–1131 (2016).

49. Lukin, D. M. et al. 4h-silicon-carbide-on-insulator for integrated quantum and nonlinear photonics. *Nat. Photonics* **14**, 330–334 (2020).

50. Guo, K. et al. Nonclassical optical bistability and resonance-locked regime of photon-pair sources using silicon microring resonator. *Phys. Rev. Appl.* **11**, 034007 (2019).

51. Faruque, I. I. et al. Estimating the indistinguishability of heralded single photons using second-order correlation. *Phys. Rev. Appl.* **12**, 054029 (2019).

52. Zielnicki, K. et al. Joint spectral characterization of photon-pair sources. *J. Mod. Opt.* **65**, 1141–1160 (2018).

53. Signorini, S. & Pavesi, L. On-chip heralded single photon sources. *AVS Quant. Sci.* **2**, 041701 (2020).

54. Xin, C. et al. Spectrally separable photon-pair generation in dispersion engineered thin-film lithium niobate. *Opt. Lett.* **47**, 2830–2833 (2022).

55. Clemmen, S. et al. Continuous wave photon pair generation in silicon-on-insulator waveguides and ring resonators. *Opt. Express* **17**, 16558–16570 (2009).

56. Du, J. et al. Demonstration of a low loss, highly stable and re-useable edge coupler for high heralding efficiency and low g (2)(0) soi correlated photon pair sources. *Opt. Express* **32**, 11406–11418 (2024).

57. Guo, K. et al. High coincidence-to-accidental ratio continuous-wave photon-pair generation in a grating-coupled silicon strip waveguide. *Appl. Phys. Express* **10**, 062801 (2017).

58. Choi, J. W., Sohn, B.-U., Chen, G. F., Ng, D. K. & Tan, D. T. Correlated photon pair generation in ultra-silicon-rich nitride waveguide. *Opt. Commun.* **463**, 125351 (2020).

59. Mahmudlu, H., May, S., Angulo, A., Sorel, M. & Kues, M. Algaas-on-insulator waveguide for highly efficient photon-pair generation via spontaneous four-wave mixing. *Opt. Lett.* **46**, 1061–1064 (2021).